Journal of Alloys and Compounds 509 (2011) 4462–4469

Contents lists available at ScienceDirect

Journal of Alloys and Compounds

journal homepage: www.elsevier.com/locate/jallcom

Corrosion of an extruded magnesium alloy ZK60 component—The role of microstructural features

Rongchang Zeng[a,*], Karl Ulrich Kainer[b], Carsten Blawert[b], Wolfgang Dietzel[b,**]

[a] College of Material Science and Engineering, Shandong University of Science and Technology, Qingdao 266510, China
[b] Helmholt-Zentrum Geesthacht, Zentrum fuer Material-und Kuestenforschung GmbH, Geesthacht D-21502, Germany

ARTICLE INFO

Article history:
Received 21 November 2010
Received in revised form 8 January 2011
Accepted 16 January 2011
Available online 22 January 2011

Keywords:
Magnesium alloys
Microstructure
Corrosion
SEM

ABSTRACT

The microstructure and corrosion behavior of an extruded magnesium alloy ZK60 bumper were investigated using optical microscopy, SEM and EDS as well as potentiodynamic polarization technique. The results show that the microstructure of the component is characterized by two distinct layers: the skin with coarse grains and the interior with fine grains. Preferential attack on the interior is attributed to the macrogalvanic corrosion between the two layers with an initial potential difference. The size and distribution of the intermetallic compounds play a crucial role in pitting corrosion and intergranular corrosion.

1. Introduction

Mg alloys are applied in the automobile industry due to their unique properties such as outstanding stiffness/weight ratio, excellent castability, good damping capacity and easy recyclability [1,2]. However, Mg alloys readily undergo severe attack in a harsh environment due to their low standard electrode potential and the quasi-passivity of their oxide layers [3–6]. The poor corrosion resistance of Mg alloys has thus limited their engineering applications [7,8]. Particularly, the corrosion rate and corrosion morphology of a structural material are major concerns for design engineers. The corrosion resistance of Mg alloys depends considerably on chemical compositions [9], heat treatments [10] and the microstructure, such as grain size, intermetallic compounds and twins [11–18]. The grain refinement in the microstructure resulting from a rapid solidification process can improve the corrosion properties of Mg–Al–Zn alloys, and their corrosion mechanism is shifted from pitting corrosion to general corrosion [13]. The surface or skin layer of die-cast AZ91D alloys with very fine grains exhibits a better corrosion resistance than its core or interior [6]. This phenomenon is attributed to a higher β-fraction and more continuous β-phase neighboring finer α-grains. Moreover, it is suggested that the ratio of the β-phase to the surrounding Al-rich α governs the localized corrosion of the aged AZ91 [14]. Compared with the ingot, die-cast material with smaller grain size and fine β-phase offers a marginally lower corrosion rate and better passivation [15]. It is noteworthy that the research work so far has essentially been focused on cast Mg alloys.

Recently, there is growing interest in the automotive industry to look at potential applications for wrought Mg alloys. These latter have excellent mechanical properties which can be achieved by a special thermo-mechanical treatment. It was reported that metallurgical manipulation, in the case of hot extrusion, decreased the corrosion resistance of AZ31B and AZ80 alloy dramatically [16,17]. But, this is not always the case. In comparison with conventional extruded AZ31 alloy, a consolidated AZ31 Mg alloy with nano-scale and sub-micron grains exhibited an accelerated corrosion due to the difference in microstructure [18].

On the other hand, the microstructure of metals exerts a significant impact on the corrosion morphology. Inter-granular corrosion (IGC), related to the microstructure and prone to widely occur in wrought Al alloys [19,20] and austenitic stainless steel [21], was rarely observed in Mg alloys [7] in spite of recent observations in AZ91 [2], AZ31B [18] and ageing AZ80 [22]. Therefore, the influence of the microstructure on the corrosion behavior of magnesium alloys has not been fully understood yet.

ZK60 is a typical wrought Mg–Zn–Zr alloy [23,24]. Zr can lead to grain refinement and is thus beneficial to the corrosion resistance of Mg alloys [5,8]. So far, no investigations of the corrosion behavior of extruded components with anisotropic microstructure have been reported in the literature. It is thus necessary to elucidate the

* Corresponding author. Tel.: +86 532 86081226; fax: +86 532 860 7921.
** Corresponding author at: Helmholt-Zentrum Geesthacht, Zentrum fuer Material-und Kuestenforschung GmbH, Geesthacht D-21502, Germany. Tel.: +49 4152 871988; fax: +49 4152 871960.
E-mail addresses: rczeng2001@yahoo.com.cn (R. Zeng), wolfgang.dietzel@gkss.de (W. Dietzel).

0925-8388/$ – see front matter © 2011 Elsevier B.V. All rights reserved.
doi:10.1016/j.jallcom.2011.01.116

corrosion mechanism, particularly the influence of the microstructure on the corrosion of extrusions. This paper aims to investigate the relationship between corrosion and anisotropic microstructure, i.e., grain size and intermetallic compounds, and to provide further insight into the corrosion mechanism of an extruded ZK60 component.

2. Methods

2.1. Microstructural observation

The material used was a wrought Mg alloy ZK60 (chemical compositions: 5.6 wt% Zn, 0. 54 wt% Zr, ≤0.003 wt% Fe, ≤0.002 wt% Ni, Mg, Bal.) bumper in the as-received condition, the type of which is intended to be utilized in automobiles (see Fig. 1) and has been prepared by an extrusion process with a heating integrated mould designed by Chongqing University in China. In order to obtain a distinct microstructure for the measurement of grain size, the specimens, designated as Samples 1#, 2#, 3# and 4#, were cut from the component along the extrusion direction (Fig. 2), and ground with SiC paper up to 2500 grit from the skin into the interior to make them with different thicknesses. After polarization tests, the specimens with a slight attack were polished to a mirror finish by a machine, and then etched in a solution containing 1.5 g picric acid, 25 ml ethanol and 5 ml acetic acid together with 10 ml water, examined by means of a Leica optical microscope. The grain size was measured using linear intercept method with the aid of Aqwinto analysis software according to ASTM E122-88. The average grain size is estimated by counting the number if grains intercepted by five straight lines sufficiently long enough to yield at least 50 intercepts. Also, microstructure and corrosion morphology were observed using Oxford and JSM-5600LV scanning electron microscopes (SEM). The latter was equipped with an energy-dispersive X-ray spectrum analyzer (EDS).

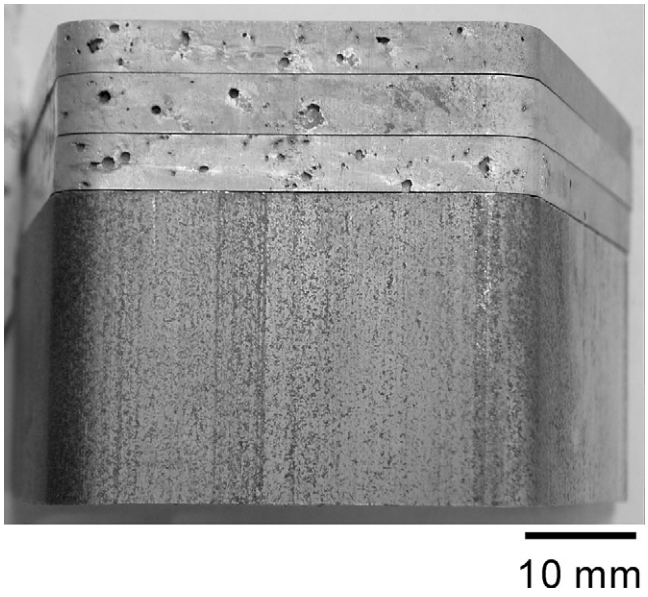

Fig. 1. Birds' view of the ZK60 bumper intended to be applied in a car, in which the three sections at the top are the cut samples after a salt spray test. The orientation of the component from bottom to top corresponds to the extrusion direction or the longitudinal direction (indicated by surface scratches).

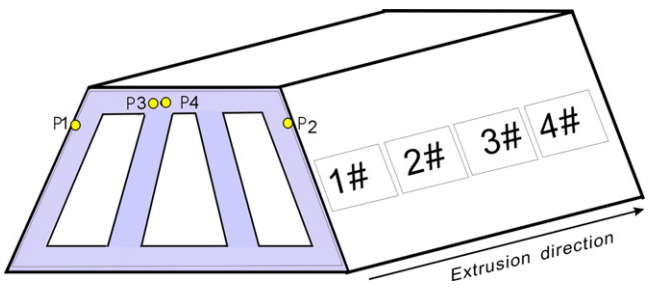

Fig. 2. Samples 1#, 2#, 3# and 4# cut from the ZK60 component along the extrusion direction shown by the arrow.

2.2. Corrosion tests

2.2.1. Conventional polarization tests

In order to evaluate the effect of grain size on corrosion resistance, the aforementioned Samples 1#, 2#, 3# and 4# were used for conventional polarization tests. First, they were ground with SiC paper up to 2500 grit, using both distilled water and acetone for the rinsing. And the surface was then dried with warm flowing air prior to electrochemical testing. Conventional potentiodynamic polarization tests were then carried out using a PS6 Meinsberg potentiostat. A three-electrode system was employed: a saturated calomel electrode (SCE) and a platinum plate were used as reference electrode together with an auxiliary electrode. The scanning voltage was ±300 mV vs. SCE relative to the open circuit potential (OCP) with an exposure area of 2.84 cm^2 and a scan speed of 0.2 mV/s. The tests were conducted after 5 min immersion in 3.5 wt% NaCl solution at room-temperature. All potentials in the study are quoted with respect to the SCE. In the Tafel extrapolation method for measuring the Mg corrosion rate, the corrosion current density, i_{corr} (mA/cm^2) is estimated by Tafel extrapolation of the cathodic branch of the polarization curve.

2.2.2. Polarization measurements using a mini cell system

In order to understand the effect of microstructure on cross-section on corrosion, it is of necessity to probe the corrosion behavior of localized regions due to the limitation of the shape and size of the component. The tested areas in this study are designated as P1, P2 and P3, P4 corresponding to the bright weld areas with coarse grains and the interiors with finer grains in cross-section direction, respectively. Here, it is difficult or even impossible for naked eyes to detect an accurate tiny location in micrometer scale. Moreover, the diameter (0.5 mm) of the plastic tip for electrochemical tests is far greater than the micrometer-scale dimensions of the welding area and the skin thickness (in P1 and P2). Thus, the locations P1 and P2 are rough or not concise and could not entirely be representative of the skin. Surely, P3 and P4 could fully represent the interior. Potentiodynamic electrochemical tests were performed in a mini cell system (MCS): A working electrode in contact with the plastic tip and filled with 3.5 wt% NaCl solution; inside, a saturated calomel electrode (SCE) and a platinum plate were used as reference electrode and auxiliary electrode, respectively. Initially, the variation in OCP with immersion time was measured in the solution for 5 min, and then the potentiodynamic polarization tests were conducted. The scanning potential ranged ±300 mV vs. SCE relative to the OCP. Compared to the conventional cell, the mini cell system employed a higher scanning rate of 10 mV vs. SCE/s to thwart rapid corrosive attack of the tiny measurement surface.

2.2.3. Salt spray tests

It is discussed [25,26] that the limitations of the use of polarization tests to estimate corrosion behavior is the anode polarization curve of magnesium alloys cannot fit for Tafel law. Therefore, salt spray tests were employed to evaluate the corrosion resistance. The samples were cut into pieces with a thickness of approximately 5 mm with a handsaw from the component in cross-sectional direction as shown in Fig. 1. And the machined surfaces were polished firstly with a file and then 2500 grit silicon carbide paper to the same surface roughness for assessing their corrosion susceptibility by employing a 5.0 wt% NaCl salt spray according to the DIN 50021 standard in a salt spray test chamber for 48 h.

3. Results

3.1. Microstructural observations

The optical micrograph of the microstructure in a cross-sectional view is shown in Fig. 3. It reveals an inhomogeneous microstructure with two distinct zones: the top outer layer or skin has merely one or two coarse grains with a size of about 100 μm, whereas the interior layer comprises fine equiaxed grains with a size of approximately 20 μm. A distinct interface between the coarse and fine grained domains is noticeable. However, the grain size in the bottom layer or the inner wall shows no apparent difference from the interiors. It is to be noted that a welding seam in bright color could be seen in natural light which was sited at the locations (1) in Fig. 3b and (2) in Fig. 3c. The seams resulted from the coalescence of the two extrusions passing the "bridge" or connection of the heating moulds. As a consequence, a seam with one coarse grain across the interior was formed.

The microstructures of the extrusion direction (Fig. 4a) are characterized by the presence of fine equiaxial grains and intermetallic compounds precipitated along the grain boundaries (GBs) and the grain interiors; within the coarse grains also some twins are apparent. The average grain size of Samples 1#, 2#, 3# and 4#, polished to some depth from the surface to the interior to make them

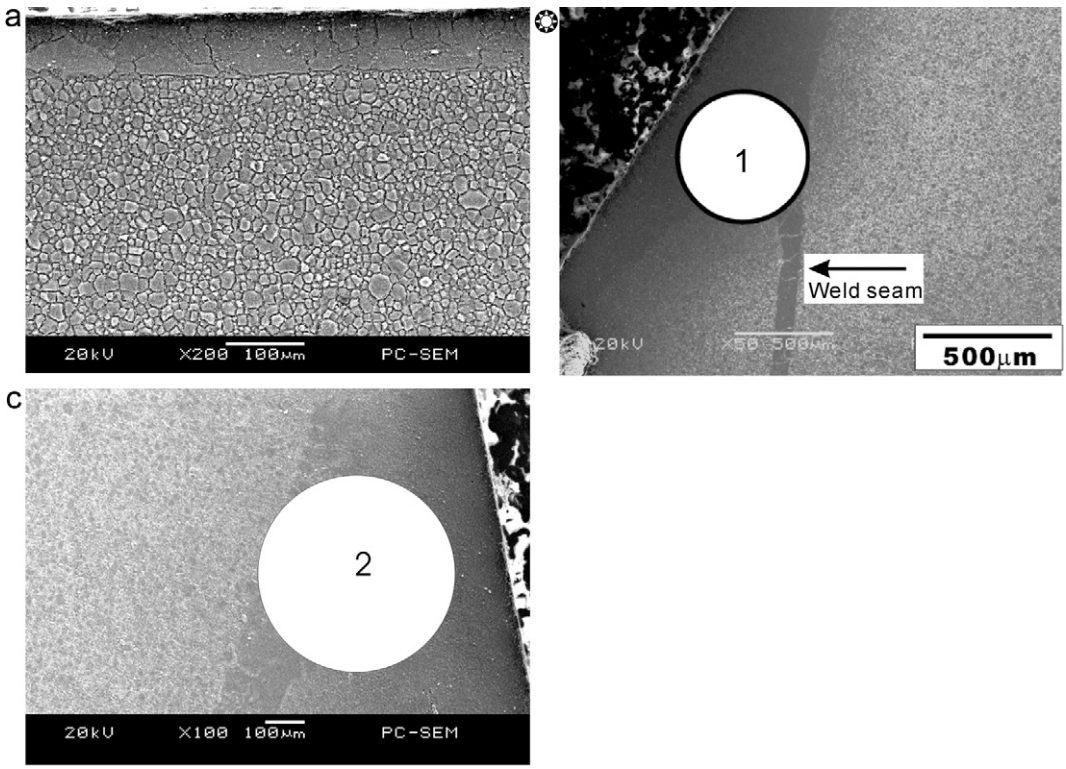

Fig. 3. SEM micrographs of the microstructure in cross-section: (a) the skin with coarse grains in contrast to the interior having fine equiaxed grains, (b and c) welding seam, resulting from the extrusion process, revealing coarse grains across the interiors. The numbers 1, 2 designate the positions P1, P2 of the figure for electrochemical measurements with MCS, respectively.

have various microstructure along the extrusion direction, corresponds to 18 μm (as shown in Fig. 4b), 16 μm, 15 μm and 11 μm, respectively.

The SEM micrograph in Fig. 5 is indicative of most intermetallic compounds precipitating along the GBs and a few in the grain interiors. These compounds, investigated by means of EDS, represent MgZn phases. The presence of Zr–Zn particles has been observed in Mg–Zn–Zr alloys [27] and $MgZn_2$ or Mg_2Zn_3 phases in Zn-containing Mg alloys [28,29]. In this study, there were two types of precipitates: the finer one existing along the GBs and also within the grain interiors, and the large one occurring at the GBs.

3.2. Corrosion morphology

Accordingly, the intermetallic compounds in magnesium alloys have a relatively higher potential as the cathode, and their neighboring α-matrix as the anode with a lower potential [7]. In the most cases reported in literature [7,8], the big difference in potentials between the matrix and intermetallic compounds results in pitting corrosion.

Pitting corrosion is one of the dominant modes of the attack on the component. Fig. 6 depicts a variety of corrosion pits observed on the cross-sectional view after a 48 h salt spray test. The corrosion pit in Fig. 6a has a round shape and is covered with oxide debris remaining on the surface. A secondary particle seen on the bottom of the pit (Fig. 6a) illustrates that pitting corrosion initiated at the large MgZn intermetallic compounds. The scale debris demonstrates that the grains firstly were undermined under the oxide layer, and consequently the oxide film collapsed until a deep pit formed. It can be found from Fig. 6b and c that severe localized corrosion occurred at the areas adjacent to the outer wall or skin. Pitting corrosion can be also found in Fig. 6b and d. The large Mg–Zn particles give rise to pitting corrosion of the ZK60 alloy. If no intermetallic compounds would have existed, the interior rather than the skin would have been preferentially attacked, as shown in Fig. 6e.

Interestingly, IGC occurred on either of the cross-sectional views (Fig. 6f). As a result, the grains were undercut and fallen out in the cross-sectional direction (Fig. 6g). IGC is also discerned in the extrusion direction as is shown in Fig. 6h.

These scenarios imply that the corrosion morphologies are predominantly influenced by the size and distribution of the intermetallic compounds.

3.3. Electrochemical corrosion measurements

In order to understand the corrosion mechanism, it was useful to apply the MCS to probe the corrosion behavior of the tiny and localized areas P1, P2, P3 and P4. The microstructure of the component at the locations P1, P2 (Fig. 3c and d) is predominantly characterized by coarse grains, whereas that of P3 and P4 (Fig. 6d) is composed of fine grains in the interior. The open circuit or free corrosion potential, E_{corr}, as a function of immersion time for these positions (plotted in Fig. 7) demonstrates that the initial E_{corr} at P1 and P2 was equal to approximately −1.64 V vs. SCE, which is remarkably higher than the potential at P3 and P4 (about −1.75 V vs. SCE). The initial potential difference, ΔE_{corr}, thus reached up to approximately 110 mV vs. SCE. At the initial stage, E_{corr} at P1 decreased slightly and fluctuated around its original level, then fell down to −1.66 V vs. SCE. After this, it slowly increased continuously. On the other hand, E_{corr} at P2 increased rapidly, then suddenly fell down to a lower value, and consequently floated around a potential of −1.63 V vs. SCE. This means that the film which had formed was severely broken and dissolved after incubation [30]. In contrast, the E_{corr} at P3 and P4 rose with increasing immersion time, and eventually the ΔE_{corr} between P1, P2 and P3, P4 was minimized so that the galvanic corrosion was not so pronounced as would otherwise be expected. As shown in Figs. 8 and 9, the corrosion current den-

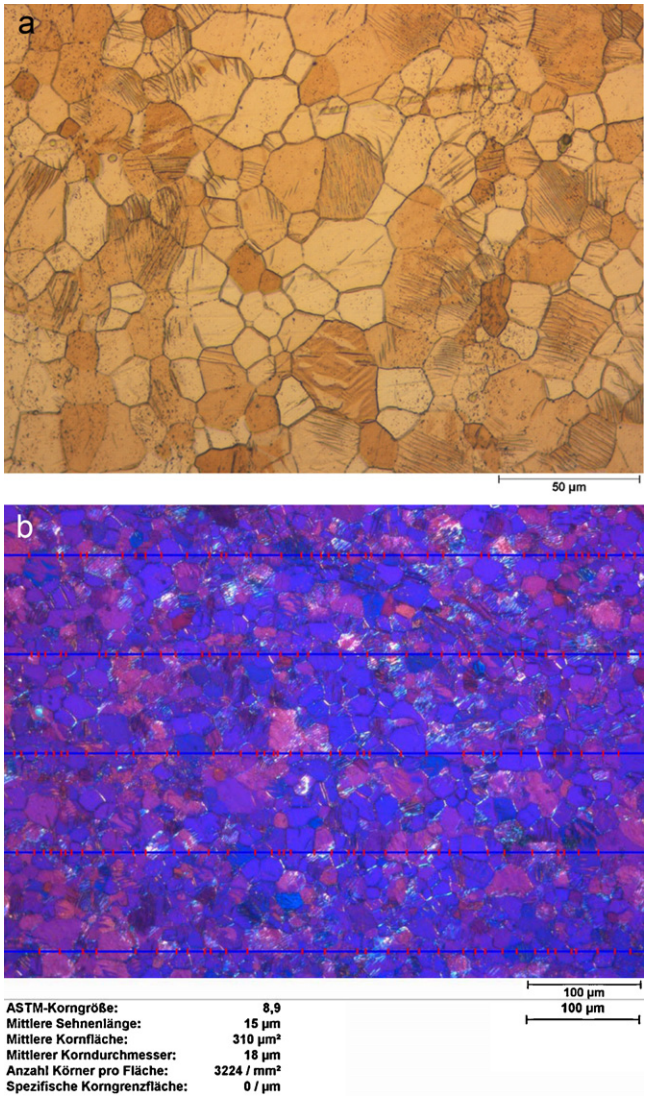

Fig. 4. (a) Optical microstructure of the longitudinal or extrusion direction, showing a much more homogenous microstructure with fine equiaxed grains than that on the cross-section and (b) metallography for grain size with linear intercept method according to ASTM standard E112-88.

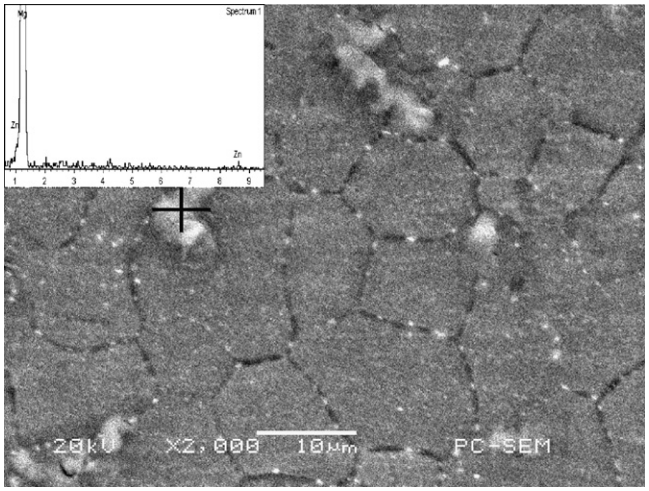

Fig. 5. SEM micrograph showing MgZn phases in white color, probed via EDS, precipitating along the grain boundaries and EDS spectra of the intermetallic compound (insert).

Table 1
Electrochemical parameters of Samples 1#, 2#, 3# and 4#.

Samples	β_c	E_{corr} (V vs. SCE)	I_{corr} (A/cm^2)
1#	96	−1.56	1.28×10^{-5}
2#	113	−1.58	1.08×10^{-5}
3#	107	−1.67	1.07×10^{-5}
4#	130	−1.57	9.50×10^{-6}

sity at P1, P2, P3 and P4 are 9.38×10^{-5} A/cm^2, 6.04×10^{-5} A/cm^2, 7.43×10^{-6} A/cm^2 and 2.57×10^{-5} A/cm^2, respectively. The corrosion current density at P1and P2 was much higher than that at P3 and P4.

The current densities at P1, P2, P3 and P4 are higher than that of Samples 1#, 2#, 3# and 4# as depicted in Fig. 10, which are 1.28×10^{-5} A/cm^2, 1.08×10^{-5} A/cm^2, 1.07×10^{-5} A/cm^2 and 9.5×10^{-6} A/cm^2, respectively. Thus, the attack on the cross-section is much more serious than the extrusion direction.

4. Discussion

4.1. Influence of grain size on corrosion rate

It is well recognized that the smaller the grain size the better is the corrosion resistance of Mg–Al alloys [16]. The question was whether would be the same for the Mg–Zn–Zr alloy. The corrosion rate, which was evaluated by conventional polarization test, as a function of grain size for the extruded ZK60 alloy in the extrusion or longitudinal direction is indicated in Fig. 11. The anodic polarization curve of magnesium does not satisfy Tafel law, because hydrogen evolution and dissolution of magnesium occurred simultaneously during the corrosion of magnesium. Therefore, in the Tafel extrapolation method for measuring the Mg corrosion rate, the corrosion current density, i_{corr} (mA/cm^2) is estimated by Tafel extrapolation of the cathodic branch of the polarization curve [24,25]. In each case the cathodic branch provided an extensive linear Tafel region, the evaluated i_{corr} value is included in Table 1 as is the corresponding corrosion rate. It is evident that the finer the grains the lower the corrosion current density or the corrosion resistance. It should be noted that the above result is in pronounced agreement with the findings from polarization curves obtained in MCS in Fig. 9 and a report in the literature dealing with diecast Mg alloy AZ91 [6].

4.2. Influence of grain size on corrosion morphology

Since the aforementioned electrochemical polarization tests demonstrated that the smaller the grains the higher the corrosion resistance, the coarse grained skin (Fig. 6b–e) should have a corrosion resistance inferior to the fine grained interior. Surprisingly, the skin was hardly attacked but the interior neighboring the skin, particularly on the bend and the weld zones, was severely corroded. The scenario cannot be explained in terms of corrosion current density! Also, this case is inconsistent with the reports for die-cast Mg–Al alloys, i.e., in these alloys the interior with a coarse grained microstructure had a corrosion resistance which was inferior to the skin with a fine grained one [5,6]. Yet, it does apparently sound contradictory between findings based on corrosion morphologies after the salt fog test and our data from polarization curves in Fig. 9 and the literature somewhere [6] as well.

To better understand the mechanism of corrosion, a schematic diagram of the mechanism for the macrogalvanic corrosion between the skin and the interior of the ZK60 component is proposed as demonstrated in Fig. 12. The model can clarify the corrosion mechanism of the component on cross-section with an anisotropic microstructure. That is, it is the large variation in initial potentials between the skin and the interior that result in a macro-

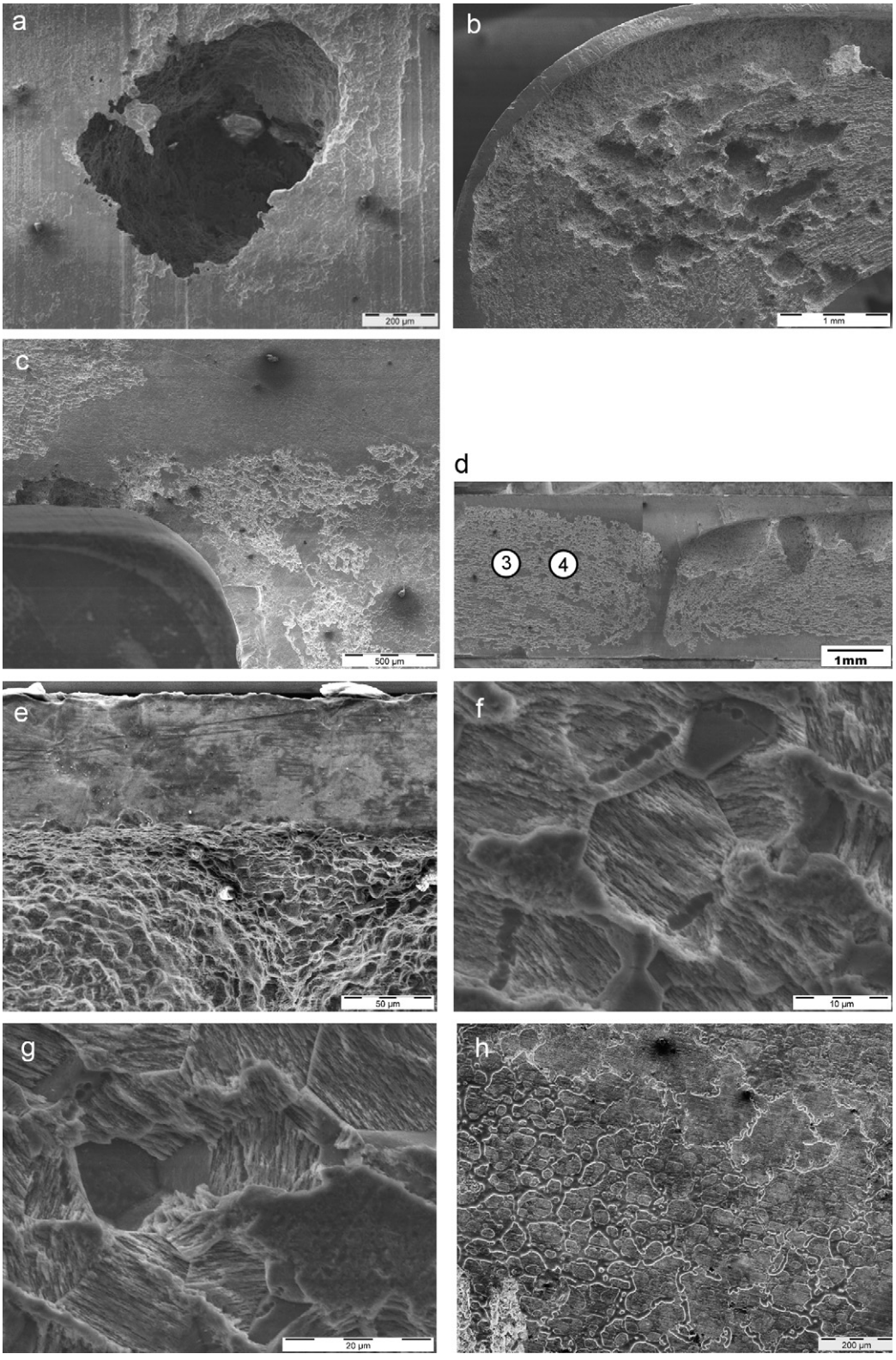

Fig. 6. SEM micrographs of the ZK60 bumper in a cross-sectional view: (a) corrosion pit, (b) serious localized corrosion evolved in the interiors, adjacent the skin with coarse grained microstructure retained on a bend, (c) severe localized attack neighboring the inner wall in a bend, (d) corrosion attack in the interior neighboring the skin and the weld seam, the numbers 3 and 4 designate the measurement positions P3 and P4 for MCS, (e) magnification of the corrosion morphology between the skin and the neighboring interior, (f) IGC; and (g) location of a grain which was undercut and fell out, and (h) grooves showing IGC also occurring in extrusion view.

galvanic corrosion and an insignificant attack at the interior (Fig. 6d and e).

Usually, galvanic corrosion can occur when two dissimilar metallic alloys are in electrical contact with each other for electron transport and are exposed to a conductive environment corrosive electrolyte [31]. The material with a lower E_{corr} in a galvanic couple becomes more active and corrodes preferentially. Corrosion severity of a galvanic couple depends upon various factors such as

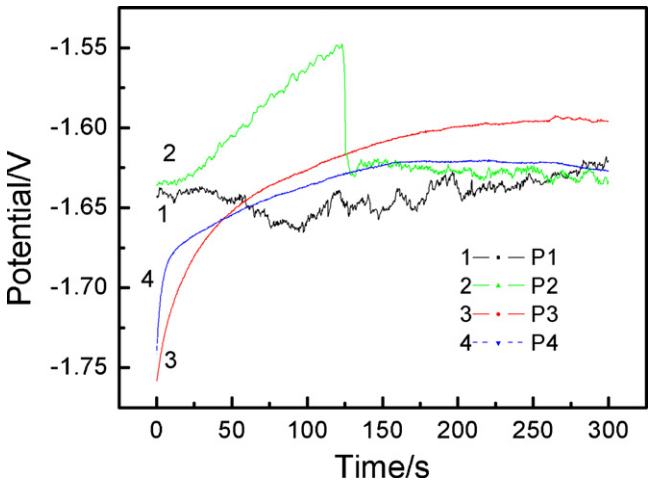

Fig. 7. Free corrosion potential, measured with MCS, as a function of immersion time for the ZK60 component in 3.5 wt% NaCl solutions for 5 min at room temperature.

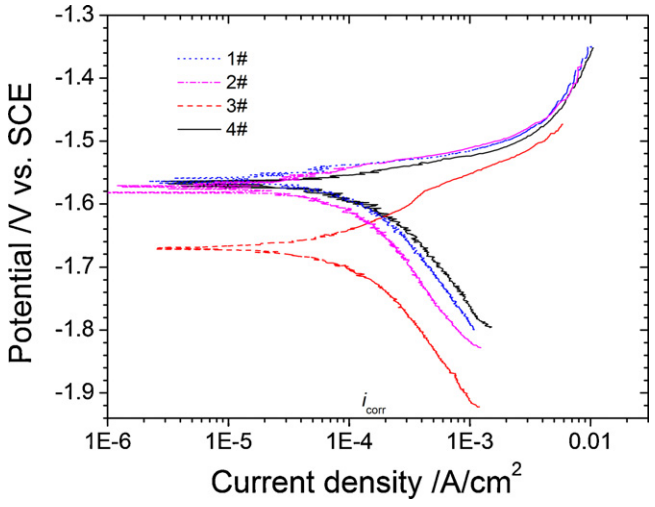

Fig. 10. Polarization curves of Samples 1#, 2#, 3# and 4# with conventional polarization technique in 3.5 wt% NaCl solutions at room temperature.

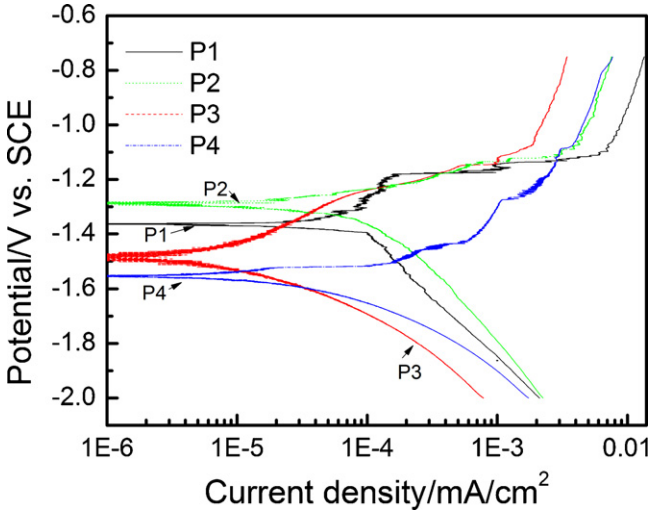

Fig. 8. Polarization curves of the ZK60 component, measured with MCS in 3.5 wt% NaCl solutions at room temperature.

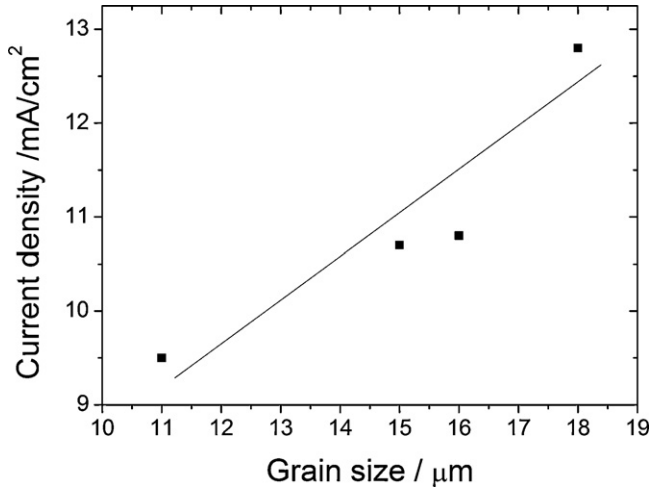

Fig. 11. Corrosion rate deserved from conventional polarization tests as a function of grain size in the extrusion direction.

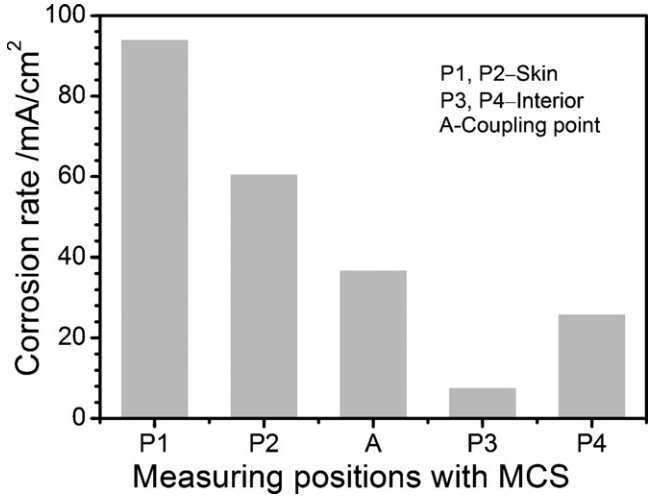

Fig. 9. Corrosion rates of various positions determined by MCS.

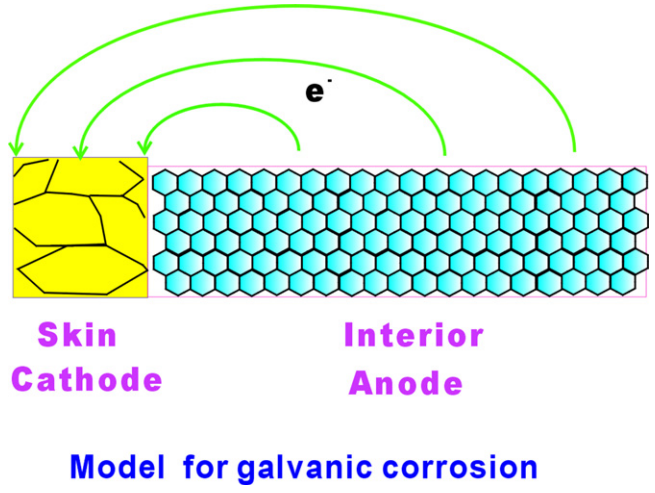

Fig. 12. Schematic diagram of the skin being protected from macrogalvanic corrosion between the skin and the interior.

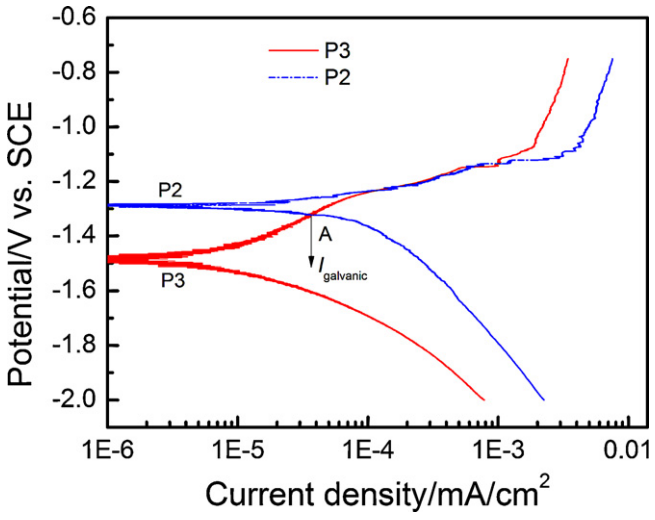

Fig. 13. An interpretation of the coupling mechanism between the interior at P3 and the skin at P2; the anodic polarization curve of P3 and cathodic polarization curve of P2 intersect at Point A.

E_{corr} difference between the two metal alloys, polarization behavior of individual alloys, anode to cathode area ratio, electrolyte conductivity, polarization characteristics of the metals involved, and distance between the coupled alloys, etc. [21]. According to the theory of galvanic corrosion [32], dissolution current density of anode (I_{a1}) or the galvanic current density (I_g) can be expressed as

$$\ln I_g = \ln I_{a1} = \frac{E_{corr2} - E_{corr1}}{b_{a1} + b_{c2}} + \frac{b_{a1}}{b_{a1} + b_{c2}} \ln I_{corr1} + \frac{b_{c2}}{b_{a1} + b_{c2}} \ln I_{corr2} + \frac{b_{c2}}{b_{a1} + b_{c2}} \ln \frac{A_2}{A_1} \quad (1)$$

where b_{a1} and b_{c2} are Tafel slopes of anodic reaction and cathodic reaction of anodic material, respectively; E_{corr1} and E_{corr2} are free corrosion potential of anode and cathode, respectively; I_{corr1} and I_{corr2} are free corrosion current of anode and cathode, respectively; A_1 and A_2 are area of anode and cathode, respectively.

If ΔE_{corr}(=$E_{corr2} - E_{corr1}$) is higher than 50 mV, there is a risk of an increased corrosion rate of the less noble metal after galvanic coupling [33]. As stated above, ΔE_{corr} between the skin and the interior at the initial state hit 110 mV. The skin was more noble and the cathode, the interior was more active and hence formed the anode. In a corrosive environment both formed a galvanic couple. The galvanic corrosion rate can roughly be predicated by superimposing the polarization curves of the anodic and cathodic materials [34]. When the open-circuit potentials of the anode and cathode are relatively far apart, more than about 120 mV, depending on the slopes of the curves, this predication is fairly accurate. The intersection of the anodic curve for the anodic material with the cathodic curve for the cathodic material provides an indication of the galvanic corrosion rate, $I_{galvanic}$, and the coupled potential, E_{couple} [34].

When a metallic contact is made between a more noble metal and a less noble one, the corrosion rate of the latter will increase and that of the former will decrease. Assuming that the interior, i.e., P3, and the skin, i.e., P2, are coupled together (as shown in Fig. 13), the anodic polarization curve of P3 and the cathodic polarization curve of P2 would intersect at Point A. The corrosion current density of the interior at P3 would then increase by one order of magnitude from 7.43×10^{-6} A/cm^2 to 3.66×10^{-5} A/cm^2, whereas that of the skin at P2 would decrease from 6.04×10^{-5} A/cm^2 to 3.66×10^{-5} A/cm^2. The skin was efficiently protected and the deterioration of the interior was accelerated.

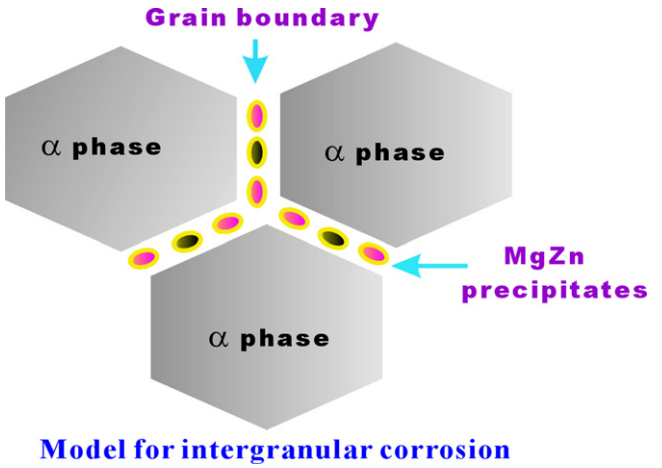

Fig. 14. Schematic diagram of the intergranular corrosion predominately caused by microgalvanic corrosion between the fine MgZn precipitates at or on GBs and the adjacent matrix.

Fortunately, the area ratio of cathode and anode in this situation is far less than one. That is,

$$A_1 \geq A_2 \quad (2)$$

$$0 < \frac{A_2}{A_1} \leq 1 \quad (3)$$

$$\ln \frac{A_2}{A_1} \leq 0 \quad (4)$$

Thus, the anode to cathode area ratio leads to a reduction in I_g, and an insignificant deterioration of the interior (Fig. 6).

4.3. *Influence of intermetallic compounds on corrosion morphologies*

The size and distribution of the intermetallic compounds exert an important impact on the corrosion morphology of the ZK60 alloy. It can be found from Fig. 6a–d that the coarse intermetallic compounds led to severe pitting corrosion either on the skin or at the interior. Unfortunately, when a large MgZn precipitate (Fig. 5) is located in the interior adjacent to the skin, the corrosion is accelerated and gives rise to more serious deterioration in the interior (Fig. 6b and d), because the potential of intermetallic compounds is more negative in comparison to that of the α-matrix [8]. It is generally observed for other Mg alloys that corrosion pits initiate at flaws adjacent to a fraction of secondary phases, such as $Mg_{17}Al_{12}$, AlMn(Fe) or Mg_2Si, as a result of the breakdown of the passivity film [5,8,30]. This is followed by the formation of an electrochemical cell in which the secondary phase particles of the type AlMn, AlMnFe, $Mg_{17}Al_{12}$, Mg_2Cu are more noble and form the cathode, while the neighboring α-Mg matrix is more active and forms the anode [7,8].

Now to the role of fine intermetallic compounds. Surprisingly, IGC, that is localized attack along the GBs, was observed in Fig. 6f–h. It is obvious that grains detached and left the pits (Fig. 6g) or grooves (Fig. 6h). This is attributable to the fine MgZn precipitates formed at the GBs (Fig. 5). Thereby, grooves occurred after 48 h salt spray test in the extrusion direction and some grains peeled off in the cross-sectional view. The schematic diagram in Fig. 14 illustrates the IGC mechanism of the extruded ZK60 alloy. The IGC results from the microgalvanic corrosion between the fine MgZn precipitates at the GBs and the adjoining the grain interiors. The fine precipitates are more noble than the bulk material; these precipitates will hence stimulate GB attack by acting as efficient local cathodes. Moreover, Zn-depleted zones probably formed surrounding the GBs, and addi-

tional internal stress was also possibly evolved along the extrusion direction. A further investigation of these issues will be required.

5. Conclusion

The microstructure and corrosion morphologies as well as their relationship of an extruded ZK60 bumper were investigated. Pitting corrosion, galvanic corrosion and IGC were simultaneously discerned. Two models for the explanation on the mechanisms of macrogalvanic corrosion and IGC resulting from microgalvanic corrosion were proposed. Following conclusions are made:

(1) The typical microstructure in the cross-section of the extruded ZK60 component exhibits two regions: an outer layer or skin with one or two coarse grains with a size of approximately 100 μm, and the interior with fine equiaxed grains having a size of about 20 μm. While on the extrusion direction, the microstructure is characterized by fine equiaxed grains with an average size of 11–18 μm, related to the depth from the surface to the interior.
(2) The corrosion rate of the ZK60 alloy increases with an increase in grain size. The initial potentials exert a very significant influence over the attack in aggressive environment.
(3) The corrosion morphology of the alloy with an anisotropic microstructure is correlated to the grain size and to the size and distribution of the intermetallic compounds. The mild attack of the skin and intergranular corrosion are attributed to macrogalvanic corrosion and microgalvanic corrosion in an aggressive medium.
(4) This investigation discloses the limitation of corrosion current density as the criterion for the evaluation on corrosion resistance. Also, the potential is the other critical criterion for the evaluation.

Acknowledgements

The authors gratefully acknowledge the technical support extended by Mr. U. Burmester, Mr. V. Kree and Ms. P. Fischer in GKSS-Forschungszentrum Geesthacht GmbH during the course of this metallurgical preparation and examination, and Dr. M. Lucia Nascimento, Fachgebiet Werkstofftechnik, Technische Universität Berlin, for her help on the corrosion tests using the mini cell system.

References

[1] K.U. Kainer, P. Bala Srinivasan, C. Blawert, W. Dietzel, Shreir's Corros. (2010) 2011–2041.
[2] J. Chen, J.Q. Wang, E.H. Han, J.H. Dong, W. Ke, Corros. Sci. 50 (2008) 1292–1305.
[3] M. Jönsson, D. Persson, C. Leygraf, Corros. Sci. 50 (2008) 1406–1413.
[4] W. Zhou, D. Shan, E. Han, W. Ke, Trans. Nonferrous Met. Soc. China 18 (2008) s334–s338.
[5] G. Song, Adv. Eng. Mater. 7 (2005) 563–586.
[6] G. Song, A. Atrens, M. Dargusch, Corros. Sci. 41 (1998) 249–273.
[7] G. Song, A. Atrens, Adv. Eng. Mater. 1 (1999) 11–33.
[8] R.C. Zeng, J. Zhang, W.J. Huang, W. Dietzel, K.U. Kainer, C. Blawert, W. Ke, Trans. Nonferrous Met. Soc. China 16 (2006) s763–s771.
[9] M. Liu, P. Schmutz, P.J. Uggowitzer, G. Song, A. Atrens, Corros. Sci. 52 (2010) 3687–3701.
[10] M.C. Zhao, M. Liu, G. Song, A. Atrens, Adv. Eng. Mater. 10 (2008) 93–103.
[11] M.C. Zhao, M. Liu, G. Song, A. Atrens, Corros. Sci. 50 (2008) 1939–1953.
[12] M.C. Zhao, M. Liu, G. Song, A. Atrens, Adv. Eng. Mater. 10 (2008) 104–111.
[13] D. Daloz, P. Steinmetz, G. Michot, Corrosion 53 (1997) 944–954.
[14] R.K. Singh Raman, Metall. Mater. Trans. A 35 (2004) 2525–2531.
[15] R. Ambat, N.N. Aung, W. Zhou, Corros. Sci. 42 (2000) 1433–1455.
[16] N.N. Aung, W. Zhou, Corros. Sci. 52 (2010) 589–594.
[17] M. Ben-Haroush, G. Ben-Hamu, D. Eliezer, L. Wagner, Corros. Sci. 50 (2008) 1766–1778.
[18] E. Aghion, A. Arnon, J. Mater. Sci. 42 (2007) 6371–6376.
[19] V. Guillaumin, G. Mankowski, Corros. Sci. 41 (1998) 421–438.
[20] J.M. Sánchez-Amaya, M. Bethencourt, L. González-Rovira, F.J. Botana, Electrochem. Acta 52 (2007) 6569–6583.
[21] C. Garcia, M.P. Tiedra, Y. Blanco, O. Martin, F. Martin, Corros. Sci. 50 (2008) 2390–2397.
[22] R.C. Zeng, E.H. Han, W. Ke, J. Mater. Sci. Technol. 23 (2007) 363–368.
[23] F. Pan, J. Mao, X. Chen, J. Peng, J. Wang, Trans. Nonferrous Met. Soc. China 20 (2010) 1299–1304.
[24] Y. Cheng, T. Qin, H. Wang, Z. Zhang, Trans. Nonferrous Met. Soc. China 19 (2009) 517–524.
[25] Z. Shi, A. Atrens, Corros. Sci. 53 (2011) 226–246.
[26] Z. Shi, M. Liu, A. Atrens, Corros. Sci. 52 (2010) 579–588.
[27] W.C. Neil, M. Forsyth, P.C. Howlett, C.R. Hutchinson, B.R.W. Hinton, Corros. Sci. 51 (2009) 387–394.
[28] Y.L. Ma, F.S. Pan, R.L. Zuo, J. Zhang, M.B. Yang, Trans. Nonferrous Met. Soc. China 16 (2006) s1888–s1891.
[29] C.J. Ma, M. Liu, G.H. Wu, W.J. Ding, Y.P. Zhu, Mater. Sci. Technol. 20 (2004) 1661–1665.
[30] O. Lunder, J.E. Lein, S.M. Hesjevik, Werkst Korros 45 (1994) 331–340.
[31] ASTM Standard G82-98, Development and Use of a Galvanic Series for Predicting Galvanic Corrosion Performance, Annual Book of ASTM Standards, ASTM International, Philadelphia, 2003.
[32] C.N. Cao, Principles of Electrochemistry of Corrosion, Chemistry Industry Press, Beijing, 2008, pp. 105–106.
[33] E. Bardal, Corrosion and Protection-(Engineering Materials and Processes), Springer, London, 2003, pp. 94–107.
[34] R. Baboian, Corrosion Tests and Standards: Application and Interpretation, second edition, ASTM International, PA, 2005, pp. 233–238.